


Hydrodynamics of a twisting flat plate: experiments and inviscid modelling using leading-edge-suction parameter

Kamlesh Joshi,¹ Carlos Soto¹ and Samik Bhattacharya¹ 

¹Mechanical and Aerospace Engineering Department, University of Central Florida, Orlando, FL, USA

Corresponding author: Samik Bhattacharya, samik.bhattacharya@ucf.edu

(Received 14 October 2024; revised 23 April 2025; accepted 13 July 2025)

Natural fliers and marine swimmers twist and turn their lifting or control surfaces to manipulate the unsteady forces experienced in air and water. The passive deformation of such surfaces has been investigated by several researchers, but the aspect of controlled deformation has received comparatively less attention. In this paper, we experimentally measure the forces and the flow fields of a flat-plate wing (aspect ratio (AR) = 3), translating at a constant Reynolds number (Re) of 10 000, with a dynamically twisting span. We show that the unsteady forces can be dependably estimated by a three-dimensional discrete vortex model. In this model, we account for the leading-edge separation with the help of the leading-edge-suction parameter. Experiments are conducted for two angles of attack (AoAs), 5° and 15° . In addition, two rates of twisting are implemented where part of the leading edge, closer to the tip region, is twisted away from the incoming flow, increasing the effective AoA. The results show that twisting away from the flow augments the lift forces in all cases, although the rate of increase of lift is higher for the highest twist rate. The act of twisting causes an increase in effective AoA beyond the static stall angle in the AoA = 15° case. This is highlighted by a distinct dip in the force data following the initial rise after twisting is activated. The increase in effective AoA from the reference case (without twisting) causes separation of the flow below the mid-span. This, in turn, creates higher levels of vorticity in those regions and results in a leading-edge vortex with increased cross-section and strength when compared with the reference case without twisting. Finally, we apply force partitioning and reveal that dynamic twisting leads to a localised increase in vorticity-induced forces along the twisted part of the span, which is approximately twice that of the untwisted case.

Key words: flow-structure interactions, vortex dynamics, separated flows

1. Introduction

Many natural fliers and swimmers can twist their wings and fins to improve propulsive efficiency. Birds, such as the albatross, swift and hummingbird, can twist their wings to adapt to varying flight conditions efficiently (Lentink *et al.* 2007; Ingersoll & Lentink 2018; Wei, Weigang & Bifeng 2024). Insects, with their small size and high wing beat frequencies, employ dynamic twisting to generate the necessary lift and thrust for sustained flight (Jongerius & Lentink 2010; Zheng, Hedrick & Mittal 2013; Noda, Nakata & Liu 2014; Wootton 2020). In spite of these known benefits, the experimental measurements of the forces and the flow field of a dynamically twisting wing have been scarce. Moreover, there is a need to test the effectiveness of the existing reduced-order models for the prediction of the forces on a finite wing dynamically twisting along the span. In this paper, we focus on bridging these gaps by first experimentally measuring the unsteady forces and the vorticity field of a translating wing undergoing dynamic spanwise twisting. Then, we develop an analytical model using a three-dimensional discrete vortex model, which accounts for leading-edge separation.

The effects of the passive deformation of a wing on the resultant fluid–structure interaction (FSI) have been studied by several researchers, both from the biological community and the fluid dynamics community. A number of biologists have investigated the effect of wing deformation on insect flight (Grodnitsky & Morozov 1993; Dickinson, Lehmann & Chan 1998; Dickinson, Lehmann & Sane 1999; Ellington 1999; Dudley 2002). Insect wings have no muscles, so the wing deformation is always passive (Combes & Daniel 2003). Daniel & Combes (2002) showed that insect wings deform mainly under inertia–elastic forces rather than aerodynamic pressures. Nakata & Liu (2012) performed computational studies on the effect of passive flexibility on a hovering hawkmoth. Their results showed that dynamic bending delayed the breakdown of the leading-edge vortex (LEV) and augmented the lift force. Moreover, combined bending and twisting of the wing modified the wing kinematics in the distal area and enhanced the lift force immediately before stroke reversal.

The effectiveness of passive flexion has also been observed by many researchers in the fluid dynamics community who have performed experiments in wind tunnels or water tunnels with airfoils or flat plates. Heathcote & Gursul (2007) used a heaving chordwise flexible wing in a water tunnel and showed that flexibility improved both the thrust coefficient and propulsive efficiency. In another study, the same authors used a spanwise flexible wing with a heaving motion inside a water tunnel (Heathcote *et al.* 2008). They found that spanwise flexibility increased the efficiency for a Strouhal (St) number range of $0.2 < St < 0.4$. In a detailed study, Kang *et al.* (2011) performed numerical FSI analysis on wings with chordwise, spanwise and isotropic flexibility. Their study revealed that the optimal propulsive efficiency is achieved when flapping at approximately half of the natural frequency.

The aspect of active and controlled deformation of wings on FSI has been relatively less explored. Bouard, Jardin & David (2024) used Direct Numerical Simulation (DNS) to study the effect of passive and active deformation on a hovering flexible flapping wing. They showed that active deformation can improve both the lift and efficiency for a certain phase lag with the main flapping motion. Dong *et al.* (2024) performed a numerical simulation based on a hummingbird-like flapping wing model where spanwise dynamic twisting was implemented. Their results revealed that dynamic twists can lead to a higher time-averaged thrust and vertical force. Tu *et al.* (2020) investigated the twist morphing of a pitching–rolling plate and reported that the propulsive efficiency was optimised for a morphing amplitude of 120° . Cong *et al.* (2023) investigated a combined heaving and

pitching motion of a flapping wing numerically and showed that active morphing of the chord leads to improved thrust and lift by delaying the shedding of the LEV. Soto & Bhattacharya (2023) conducted an experiment where a 3D printed wing was dynamically twisted during periodic plunging kinematics. The dynamical twisting showed significant control of the forces depending on the direction of twisting. When the plate was twisted in the direction of the heave (forward twist), a near-constant lift coefficient was reported during the transition between downstroke and upstroke.

Modelling the unsteady forces of a dynamically twisting plate is still a challenging task. Many unsteady aerodynamic models, such as Theodorsen's model and Wagner's model, are based on the assumptions of attached flow and low angle of attack. Although, few researchers have developed nonlinear unsteady models for high-angle-of-attack applications as well (Leishman 1989; Leishman & Beddoes 1989; Taha, Hajj & Beran 2014; Yan, Taha & Hajj 2014; Taha *et al.* 2021; Pla Olea & Taha 2024). To account for the leading-edge separation and for the forces created by the LEV, Ramesh *et al.* (2014) developed a discrete vortex method (DVM,) which utilised point vortices shed from the leading edge. This vortex was shed whenever the leading-edge suction (quantified by the leading-edge-suction parameter, or LESP) exceeded a fixed value, termed the critical LESP. They subsequently showed that the inclusion of this LESP concept in a DVM successfully predicted the forces on a wing for a variety of unsteady kinematics. In a later paper, Martínez-Carmena & Ramesh (2024) applied a similar DVM to airfoils with a dynamically morphing camber line. This morphing discrete vortex model resulted in a better prediction of forces compared with a rigid camber line. Kumar, Padhee & Samanta (2024) recently used DVM to study the forces on a wing that had bend–twist coupling. Their approach was similar to panel methods as they divided the surface areas into multiple panels. Recently, Cavanagh, Bose & Ramesh (2024) applied the LESP-modulated DVM (LDVM) to wings with three different sweep angles. The predicted force values were successfully matched with DNS data. In spite of this recent surge in effort to apply LDVM to three-dimensional flows, a low-order model for a dynamically twisting wing is still lacking. In this paper, we have successfully applied LDVM to a dynamically twisting plate.

In this paper, we experimentally measure the unsteady forces and the flow field of a flat-plate wing that is dynamically twisting along the span as it translates along a straight line at a constant speed. The direction of twisting was opposite to the towing direction such that the effective angle of attack (AoA) increased along part of the span. The organisation of the paper is as follows. We describe the experimental set-up in § 2. After that, we first discuss the evolution of the lift and drag forces experienced by the flat-plate wing at a Reynolds number (Re) of 10 000 in § 3.1, followed by the vorticity fields of the spanwise vortices in § 3.2 and the tip vortices in § 3.3. Next, we discuss the circulation growth in the LEVs and trailing-edge vortices (TEVs) formed over the plates (§ 3.4). Finally, we present a mathematical model based on discrete vortex methods to estimate the unsteady forces on the twisting plate (§ 4).

2. Experimental details

2.1. Towing tank, flat plate and the twisting mechanism

The experiments are conducted inside a water-towing tank with a cross-sectional area measuring $1 \times 1 \text{ m}^2$ and a length of 6 m, at the University of Central Florida (figure 1). The flat-plate wing is fabricated through 3D printing employing the polyjet technique with black Agilus material, possessing a hardness rating of 70 on the Shore A scale. The flat

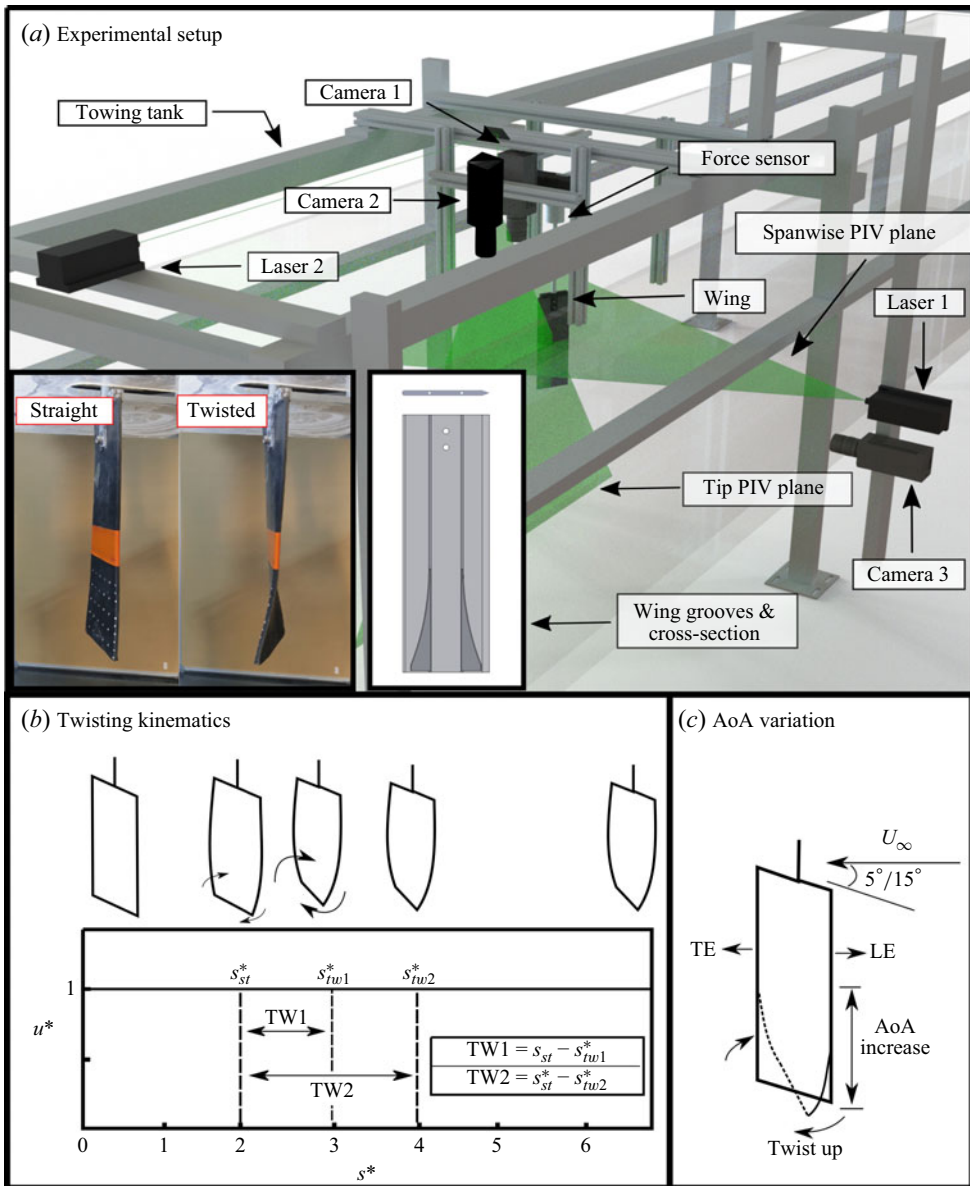


Figure 1. Details of the experiment. (a) The experimental set-up includes a force sensor and a two-camera system for particle image velocimetry (PIV); (inset) the straight and the twisted flat-plate wing and the cross-section of the plate. (b) A plot of the experimental kinematics showing the initial and final positions of the twisting manoeuvre for two twist rates, twist-1-chord and twist-2-chord. (c) A schematic illustrates the variation in the AoA along the span, leading edge and trailing edge.

plate has a chord length (c) of 10 cm with a wingspan of 30 cm (aspect ratio of 3, denoted as AR3). The plate has a rounded leading edge, and a sharpened trailing edge. It also has two internal grooves for accommodating prebent steel rods with a diameter of 3 mm. These steel rods are affixed to a pair of servo motors. Upon rotation, these motors induce a curvature in the plate's wingspan. The mechanical arrangement is designed to yield a flexion ratio of 0.6.

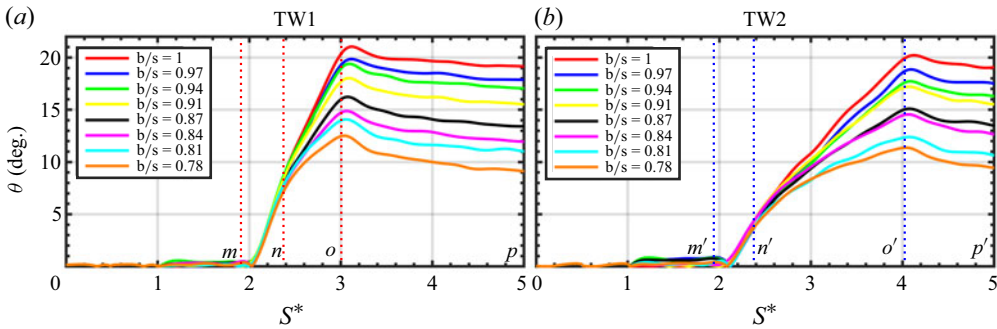


Figure 2. The θ_{twist} values obtained from DLTdv experiment for (a) twist-1-chord and (b) twist-2-chord. The twisting action begins at m in (a) (m' in (b)) and ends at o (o' in (b)). The twist rate between m (m') and n (n') is higher than that between n (n') and o (o').

2.2. Wing kinematics

The flat plates are towed along the length of the water tank using a servo-driven linear stage (HPLA80, Parker Motion, USA). The linear stage is controlled by an AC Servo controller (Applied Motion SV200, USA) and operated using Applied Motion's SVX Servo Suite software. A pulse generator (Model 9424, Quantum Composer, USA) is used to time and distribute trigger signals to the various motors and sensors in the experimental set-up (figure 1a).

The twisting manoeuvres are executed at two AoAs, specifically 5° and 15° , while maintaining a consistent velocity of 0.1 m s^{-1} , corresponding to a Reynolds number (Re) of 10 000. To avoid the initial starting transients in the force data and to ensure that the wing reaches a constant speed, the wing is moved two chord lengths before we start logging the force data. This starting point of the force record is denoted as $s^* = 0$. Two distinct twisting manoeuvres are carried out. In the first case, the flat-plate wing is twisted to the maximum twist amplitude for one chord length of travel. This case will be denoted as twist-1-chord in the rest of the paper. In the second case, denoted as twist-2-chord in the paper, the wing is twisted to the same twist amplitude during two chord lengths of travel (figure 1b). Naturally, twist-1-chord involves the highest twist acceleration. In both twisting manoeuvres, the AoA is progressively increased in the spanwise direction (figure 1c).

2.3. Twist profile measurements

The twist profile of each plate is measured using a stereoscopic imaging technique. A grid of markers is placed on the wing surface (inset, figure 1a), near the tip region. The twisting motion is performed and recorded using two high-speed cameras (PCO.edge 5.5, PCO, USA) set to capture images (resolution $1920 \text{ pixels} \times 1080 \text{ pixels}$) at 200 Hz. Three-dimensional (3-D) tracking of the marker grid nodes is performed using DLTdv, a MATLAB-based digitising tool. These 3-D positional data are then used to compute the time-varying twist angle distribution along the span.

Figure 2 shows the θ_{twist} values for the two twisting manoeuvres, i.e. twist-1-chord (figure 2a) and twist-2-chord (figure 2b). For both twisting manoeuvres the final twist angle is same. For the twist-1-chord the duration of twisting is around 1 chord, which leads to higher initial acceleration during twisting when compared with twist-2-chord.

2.4. Force sensor measurements

Force measurements are performed using a 6-degree-of-freedom force sensor (Mini 40, ATI, USA). The sensor is mounted along the shaft that holds the plate, such that the

sensor's central axis is co-linear with the plate's pitch axis. Force data are sampled at 5000 Hz using a NI USB-6216 data acquisition system (National Instruments, USA). The force data are low-pass filtered with a cutoff frequency of 6 Hz and is ensemble averaged over 20 runs.

2.5. Particle image velocimetry

Planar PIV is employed to measure the velocity field. Two separate laser sheets, each with a thickness of approximately 2 mm, are created along horizontal (spanwise) and vertical (chordwise) planes. The laser sheets are generated by 2 W continuous-wave laser heads (Dragonlaser, China). The PIV is performed at spanwise positions of 95 %, 93 %, 90 %, 86 %, 81 %, 75 %, 68 % and 60 % span, to investigate the impact of twisting manoeuvres on the LEV and the TEV. Additionally, PIV measurements are conducted on three planes near the wing tip, with adjacent planes spaced $0.07c$ (c is chord) apart, to examine the effect of twisting manoeuvres on tip vortex development. These tip vortex measurement planes are oriented at a 20° angle counterclockwise from the direction of motion. The spanwise PIV data are captured using two high-speed cameras (PCO.edge 5.5, PCO, USA), operating at a frame rate of 200 Hz while moving with the traverse system. These two sets of images are later stitched to represent both the LEV and the TEV in the same frame. The field of view for all cases measured $11.33 \text{ cm} \times 20.15 \text{ cm}$. The acquired PIV data are processed using the PIVlab software package (Stamhuis & Thielicke 2014). The processing involves a multipass approach, culminating in a $32 \text{ pixel} \times 32 \text{ pixel}$ window size with 75 % overlap. Subsequent post-processing tasks are executed using MATLAB. Vorticity calculations are derived from ensemble averaging five distinct PIV runs for each experimental condition. To quantify the sectional growth rate of wake vortices over time, the non-dimensional circulation ($\Gamma^* = \Gamma/U_\infty c$), Free stream velocity (U) within the vortex core is determined at various time points. This analysis employs the Γ_2 criteria, as outlined by Laurent Graftieaux, Michard & Grosjean (2001).

2.6. Dye-flow visualisation

Limited sets of dye-flow visualisation experiments are performed to reveal the structure of the tip vortices. Fluorescent dye is injected at the tip from the pressure side of the wing closer to the tip region. The dye is injected using tygon tubing attached to a hand-held syringe. A UV light is used to illuminate the flow field. The videos are captured with a GoPro camera at 30 Hz frame rate. Frames are later extracted from the video for comparisons among different twist cases.

3. Results and discussion

3.1. Unsteady lift and drag forces

The unsteady lift and drag forces experienced by a dynamically twisted plate of $AR = 3$ are compared with a straight plate of similar AR in figures 3 and 4, respectively. The evolution of coefficients of lift (C_l) and drag (C_d) are presented with the non-dimensional distance, S^* , travelled by the wing ($S^* = (U_\infty * t)/c$, where U_∞ is the free stream velocity, t is time and c is the chord). For the calculation of C_l of the twisted plate, the area of the untwisted (straight) plate is considered as the reference area. We consider two twisting rates, twist-1-chord and twist-2-chord for each initial AoA. In both twist-1-chord and twist-2-chord cases, the twisting starts at $S^* = 1.8$. However, in the former case, it continues until $S^* = 2.8$, whereas for the latter, it continues until $S^* = 3.8$.

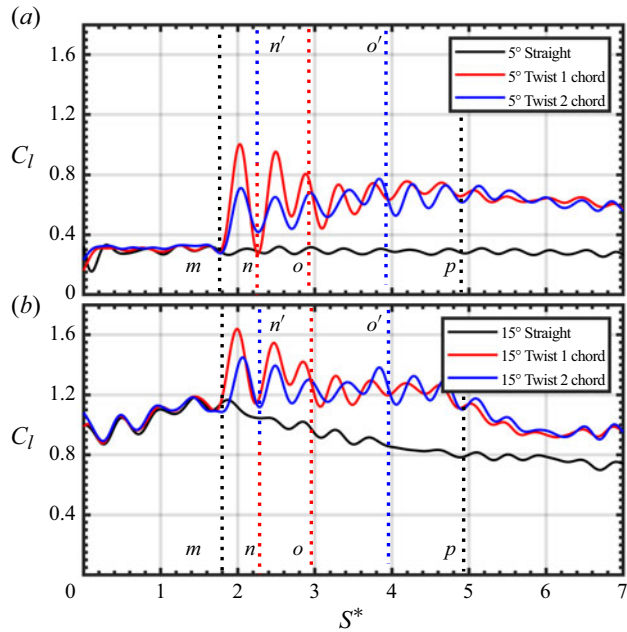


Figure 3. Comparison of the evolution of coefficient of lift (C_l) between the no-twisting case and the spanwise-twisting case for $AR = 3$ plate at $Re = 10$ k: (a) for initial AoA = 5° ; (b) for initial AoA = 15° .

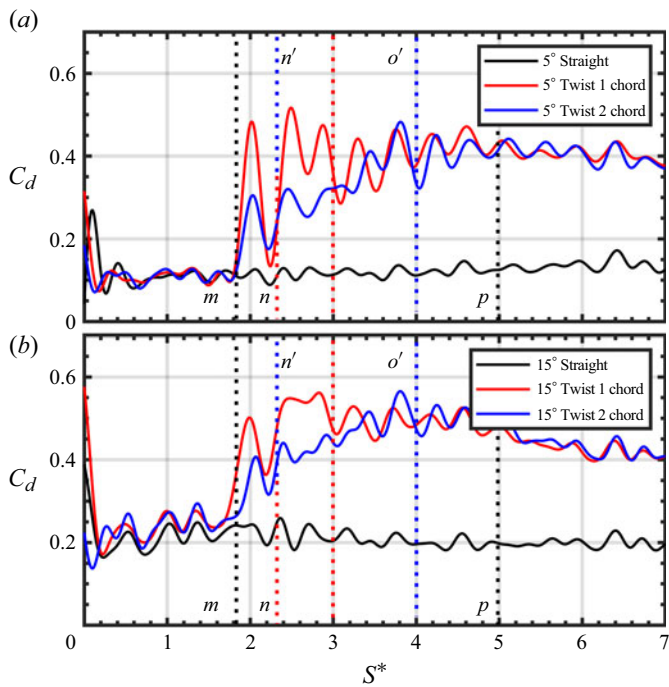


Figure 4. Comparison of the evolution of coefficient of drag (C_d) between the no-twisting case and the spanwise-twisting case for $AR = 3$ plate: (a) for initial AoA = 5° ; (b) for initial AoA = 15° .

Figure 3 shows that the onset of dynamic twisting caused both the lift and the drag coefficients to shoot up from the straight case. The sudden rise is caused by the inertial response of the wing due to the action of twisting. As twisting starts from rest, a definite amount of acceleration is required for the twisting. This sudden acceleration causes the forces to shoot up as an inertial response. In the twist-1-chord case, this acceleration is higher as the wing tip needs to twist to the maximum AoA in a smaller amount of time. Moreover, figure 2(a) shows that the rate of twist (slope) between m and n is higher compared with that between n and o . Also, the slope of the line between m and n is higher than that between m' and n' , which is expected because of the faster twist in the former case. Accordingly, the initial transients have higher peak values (red trace) in the twist-1-chord case. The action of twisting also increases the AoA for part of the span below the flexion point. Also, the wing stays twisted after the completion of the dynamic twist (2 (a) between o and p). For this reason, the eventual lift coefficients are much higher than that of the straight case. The evolution of lift of the untwisted wing with an initial AoA of 5° shows that the flow was almost attached (figure 3a). However, in the case of an initial AoA of 15° (figure 3b), the C_l traces show an upward movement until $S^* = 1.8$, which is followed by a downward slope. This trend is probably related to the formation of an LEV and its eventual shedding, even for the straight case. Moreover, in the AoA of 15° case, the wing attains a higher post-stall AoA after twisting is completed. Massive leading-edge separation due to such high AoA caused LEV formation and eventual shedding. This is evident in the eventual roll-off of the force traces. In the higher AoA case, the difference in the final C_l values between the twisting and no-twisting cases is comparatively less than the AoA = 5° case.

The drag coefficients also experience a sharp increase due to the dynamic twisting (figure 4). The final values of the drag coefficients for both twisting cases are much higher than the no-twisting case for both initial AoAs (figure 4a,b). However, between twist-1-chord and twist-2-chord cases, the final value ($C_d = 0.4$) is comparable at $S^* = 6, 7$. The increase in drag is due to the increase in the effective area facing the flow due to the twisting. However, after the end of twisting at $S^* = 2.8$ in the 15° case, C_l is approximately 1.2, i.e. almost double the C_l at similar S^* in the 5° initial AoA case. This clearly denotes that the overall lift-to-drag ratio improves due to an increase in the initial AoA while the span is twisted dynamically. The increase in drag for the twist-2-chord is more gradual due to the larger duration of twisting in this case.

3.2. Development of leading- and trailing-edge vortices

In this section, we illustrate the effect of controlled spanwise twisting on the LEV and TEV development on the $AR = 3$ wing. Comparisons are made in terms of normalised spanwise vorticity contours (ω_z^*) obtained at multiple span locations. In all the figures presented in this section, the first slice (towards the top of the wing) of the vorticity contours represents the 60 % span location, whereas the last slice represents the 95 % span. The other slices represent 68 %, 75 %, 81 %, 86 %, 90 % and 93 %, respectively. Figure 5 shows the difference in the development of spanwise vorticity over the $AR = 3$ plate, held at an AoA = 5° , between the no-twisting case and the twist-1-chord case. For the no-twisting case, only one time instant ($S^* = 2$) is presented as there are no significant differences in the spanwise non-uniformity of ω_z^* at other time instants. At $S^* = 2$, in the straight case, the leading-edge separation at 81 % span and beyond is negligible compared with other span locations closer to mid-span. We note that, at a low AoA of 5° , leading-edge separation may not lead to the formation of an LEV. However, the lack of vorticity is expected as several researchers have shown that the vortex cross-section thins down closer

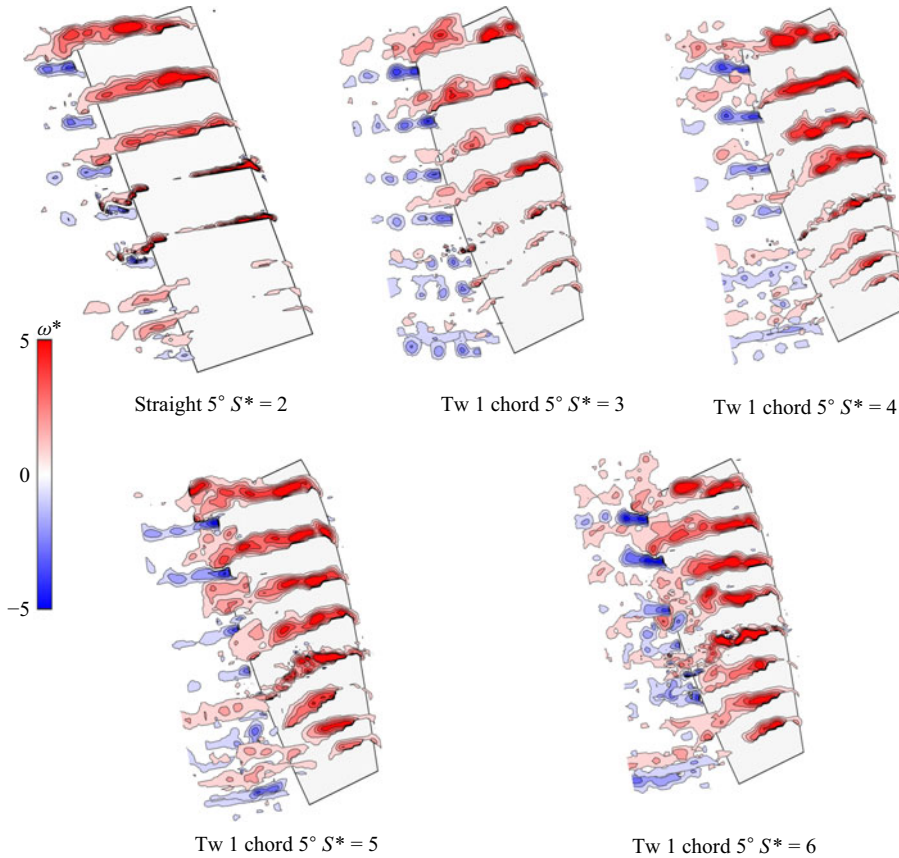


Figure 5. Contours of normalised spanwise vorticity at different span locations of the $AR = 3$ plate, and at different time instants; comparison between the no-twisting case and the twist-1-chord case for an initial AoA of $= 5^\circ$. The top of the wing represents close to 60 % span. The orientations of the wing, in this figure and later, do not follow the exact AoA in each case. Also, the wing is not drawn to scale. Rather, it is drawn for visual reference only.

to the tip owing to the hair-pin-like structure of the vortex (Linehan & Mohseni 2020; Son *et al.* 2022). In the case of dynamic twisting with a twist rate of 1-chord, however, there is significant development of the LEV closer to the tip region (figure 5). As the effective AoA increases due to the gradual twist-up motion below the 60 % span of the plate, it helps in forming LEV due to leading-edge separation. As the twisting progresses from $S^* = 2.8$ to $S^* = 3.8$, the LEV close to the tip gets stronger. Since the plate remains twisted afterward, the LEV continues to increase in size and strength beyond $S^* = 4$. Twisting also increases shedding at the trailing edge of the plate, as evident from the increased concentration of blue contours at that region. Very close to the tip, at 95 % of the span, the blue contours surely become stronger, indicating a higher level of vorticity involved.

Overall, this increase in vortical flows in the tip region of the plate is also evident for the slower twist rate case (twist-2-chord) for the same AoA of 5° (figure 6). The vortices, however, grow comparatively slower due to a slower twist rate. This fact will be more evident when we discuss the circulation growth later. A qualitative comparison of the vorticity contours at $S^* = 4$ between the two twist rates shows less concentration of blue contours in the wake region of the plate in the twist-2-chord case. Even though the distribution of the spanwise AoA is the same for both twist rates after twisting has

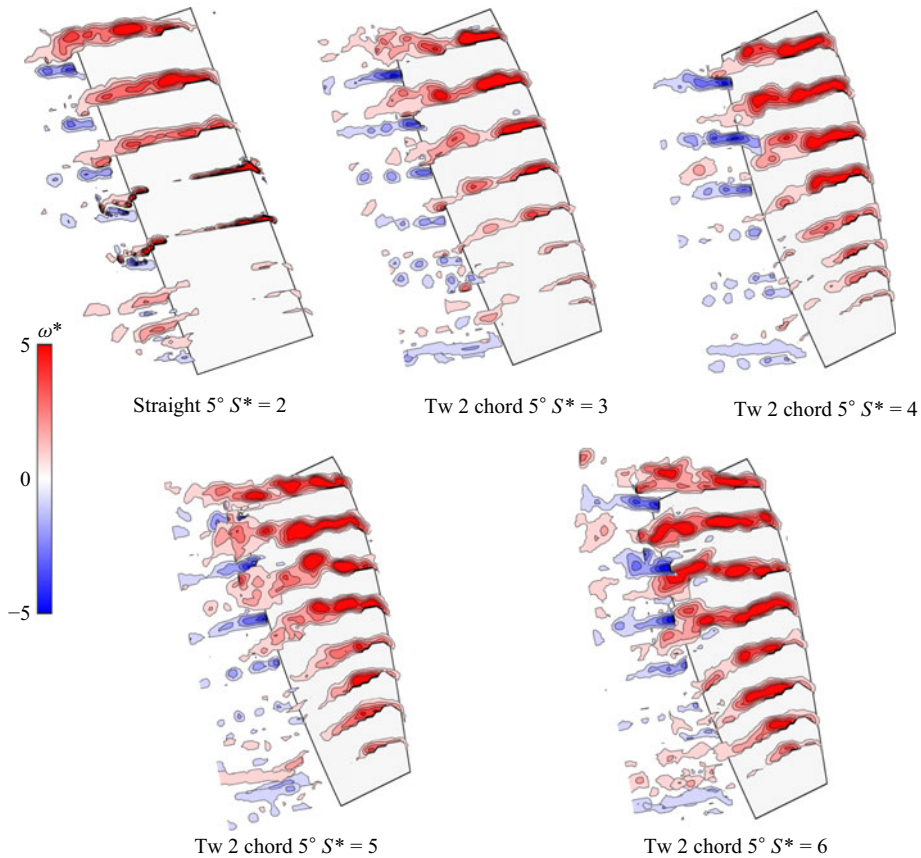


Figure 6. Contours of normalised spanwise vorticity at different span locations of the $AR = 3$ plate, and at different time instants; comparison between the no-twisting case and the twist-2-chord case for an initial AoA of 5° .

ceased, the twist-2-chord shows relatively less concentration of the TEV. This is a direct consequence of a slower twist rate, which can be explained with the help of Kelvin's circulation theorem. The rate of change of leading-edge circulation (red contours) in the twist-2-chord case being lower, the rate of TEV growth would also be lower since the TEV circulation balances the rest as per Kelvin's theorem.

When the AoA of the flat plate is increased to 15° , an increased level of vorticity development is observed over the span of the flat-plate wing. Since the AoA is 15° , flow separation at the leading edge causes strong LEV formation even closer to the flexion point, i.e. 60 % span location in the straight case (figure 7). The non-uniform distribution in the strength of the LEV is evident in figure 7 from the gradual thinning of the vorticity contours. When the plate is twisted at the fastest rate (twist-1-chord), the level of vorticity increases significantly over the whole span below the flexion point of 60 % span location. Twisting causes the effective AoA to reach a post-stall value, which leads to massive separation and larger LEV formation close to the tip compared with the straight case (figure 8). However, even with the faster twist rate, the cross-section of the LEV close to the tip of the flat plate is still negligible compared with the planes near 60 % span location at $S^* = 3$ (the twisting is completed at $S^* = 2.8$). This signifies that the formation time of the LEV at the tip region is still longer than the twisting time scale. Therefore, we can argue that the changes in the unsteady forces on the plate during twisting are caused

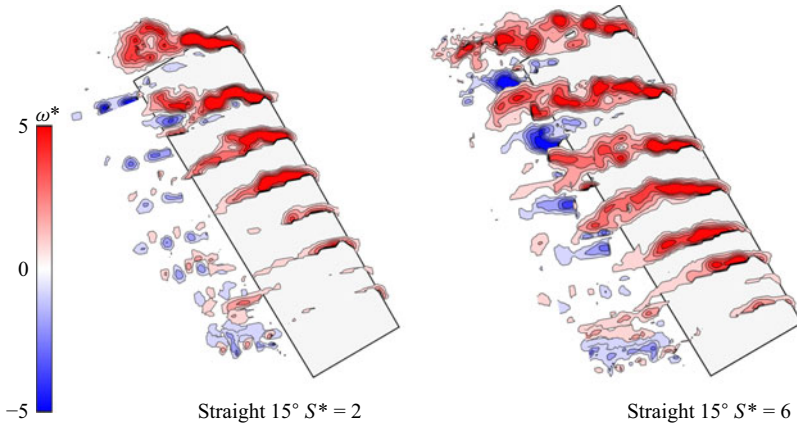


Figure 7. Contours of normalised spanwise vorticity at different span locations of the $AR = 3$ plate, and at different time instants in the no-twisting case only for an initial AoA of $= 15^\circ$.

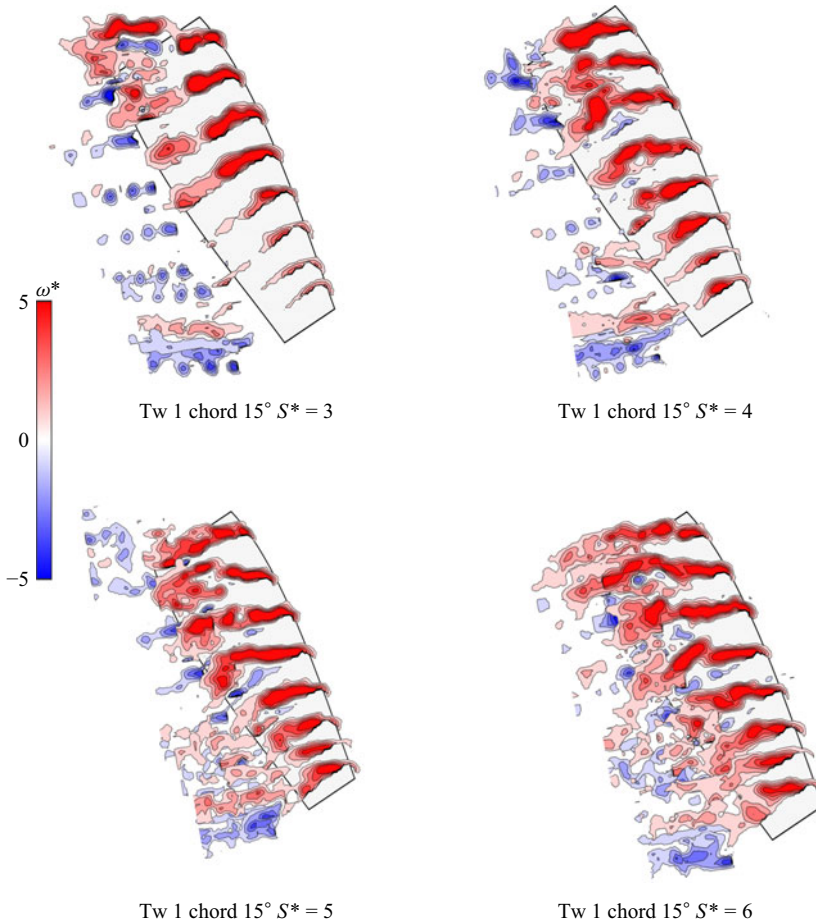


Figure 8. Contours of normalised spanwise vorticity at different span locations of the $AR = 3$ plate, and at different time instants (S^*); the twist-1-chord case for an initial AoA of $= 15^\circ$.

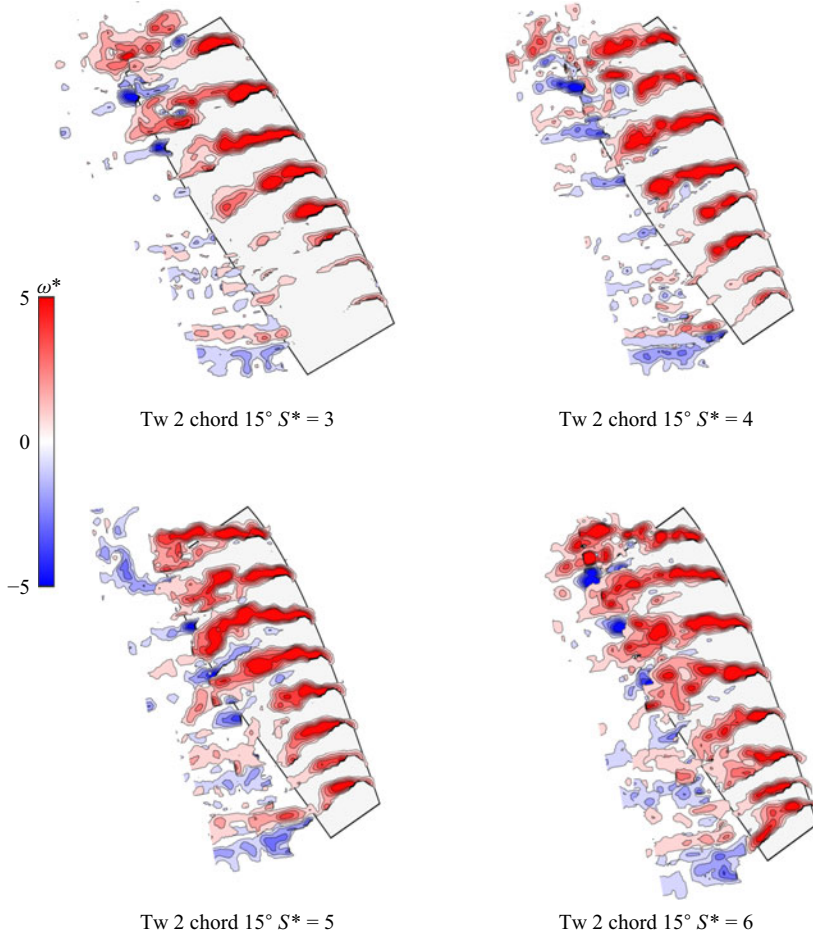


Figure 9. Contours of normalised spanwise vorticity at different span locations of the $AR = 3$ plate and at different time instants (S^*); the twist-2-chord case for an initial AoA of $= 15^\circ$.

mainly by non-circulatory effects. When the twist rate is reduced (the twist-2-chord case), similar differences are observed as in the $AoA = 5^\circ$ case (figure 9). The level of vorticity close to the tip is lower at $S^* = 4$ due to the slower twist rate. On close inspection, the faster twisting in the 15° AoA case (figure 8) shows a higher level of secondary vorticity (blue contours) on the plate surface compared with any other case at $S^* = 5, 6$, especially the ones with 5° AoA (figures 5 and 6). The formation of secondary vorticity is related to stronger LEV formation and shedding.

3.3. Development of tip vortices

We performed dye-flow visualisation as well as planar PIV to capture the development of the tip vortices. Figure 10 shows the tip vortex in the no-twisting case, which resembles a straight filament of vorticity. The tip vortex retains this straight character even at the later phases of the motion. However, the action of twisting (twist-1-chord case) bends the trajectory of the tip vortex. Figure 11 shows this deformation in the tip vortex core at $S^* = 2.6$ to $S^* = 3.1$. This severe deformation in the tip vortex causes it to diffuse at $S^* = 4.5$. We speculate that such a diffused tip vortex will cause a lower induced drag in the twist-1-chord case. The lack of a defined core of the tip vortex is due to increased

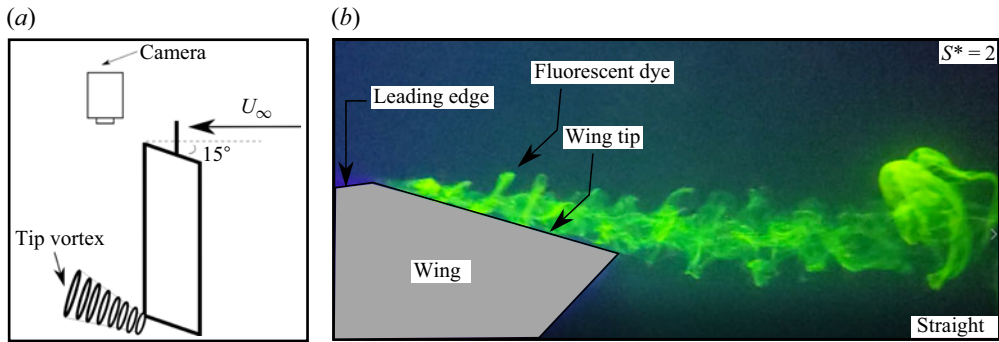


Figure 10. Dye visualisation of the tip vortex in the no-twisting case with an $\text{AoA} = 15^\circ$. The orientation of the camera and the plate (a); the straight column of tip vortex at $S^* = 2$ (b).

disturbance in the flow at the tip region. At $S^* = 4.5$, the twisting manoeuvre is complete, so the effective AoA at the tip region is more than 30° (initial AoA of $= 15^\circ + \theta_{\text{twist}}$). This causes massive separation at the tip (as proved by the vorticity contours), leading to tip stall. The diffused core of the tip vortex is a result of this tip stall.

Due to the lack of proper optical access, it was difficult to create a laser plane exactly perpendicular to the tip vortex trajectory. Instead, we created three inclined laser planes where PIV was performed. These three planes are denoted by the dotted lines in figures 12 and 13. It is evident that, due to twisting, the tip vortices got stronger and showed darker contours. This increase in circulation has been later corroborated by the circulation growth plots. This growth in tip vortex circulation can be explained by the increased level of vortical activities near the tip caused by twisting.

3.4. Growth of circulation

Figure 14 illustrates the circulation growth at four spanwise planes. The left column represents $\text{AoA} = 5^\circ$ (a,c,e,g), while the right column depicts $\text{AoA} = 15^\circ$ (b,d,f,h). In the straight case, the circulation is miniscule close to the tip in the $\text{AoA} = 5^\circ$ case. This is due to an absence of significant vortex growth as is evident from the vorticity contour plots. In all cases, the twist-1-chord manoeuvre demonstrates high circulation growth at the onset of the twisting motion, attributed to the faster twisting rate leading to strong LEV formation at the start. Conversely, the twist-2-chord manoeuvre exhibits slow and steady circulation growth. A notable dip in the growth of LEV circulation in the twist-1-case (red trace) is visible in figures 14(a,b,c,d and e). This dip suggests that the formation time of LEV is shorter for the faster twist rate case. The dip in the red trace is due to the pinching off of the LEV from the flat-plate wing. The maximum levels of circulation are consistently higher in the case of $\text{AoA} = 15^\circ$. This is expected as higher AoA will cause a larger separation leading to a bigger LEV.

The tip circulation growth is shown in figure 15. This circulation is calculated at the midplane, intersecting the tip vortex at an angle. The growth of circulation in figure 15 follows a similar trend to the growth of the LEV circulation at the 86 % and 68 % planes, shown in figures 14(h) and 14(d), respectively. Due to the twisting manoeuvre, the tip circulation is higher compared with the straight case for both manoeuvres. Between twist-1-chord and twist-2-chord, the growth rate of the circulation is consistently higher at the start for twist-1-chord, as observed in all other circulation plots. However, a notable difference is observed between the circulation growth of LEVs and the tip vortex during the twisting manoeuvre. For the tip vortex, the change in circulation (compared with the

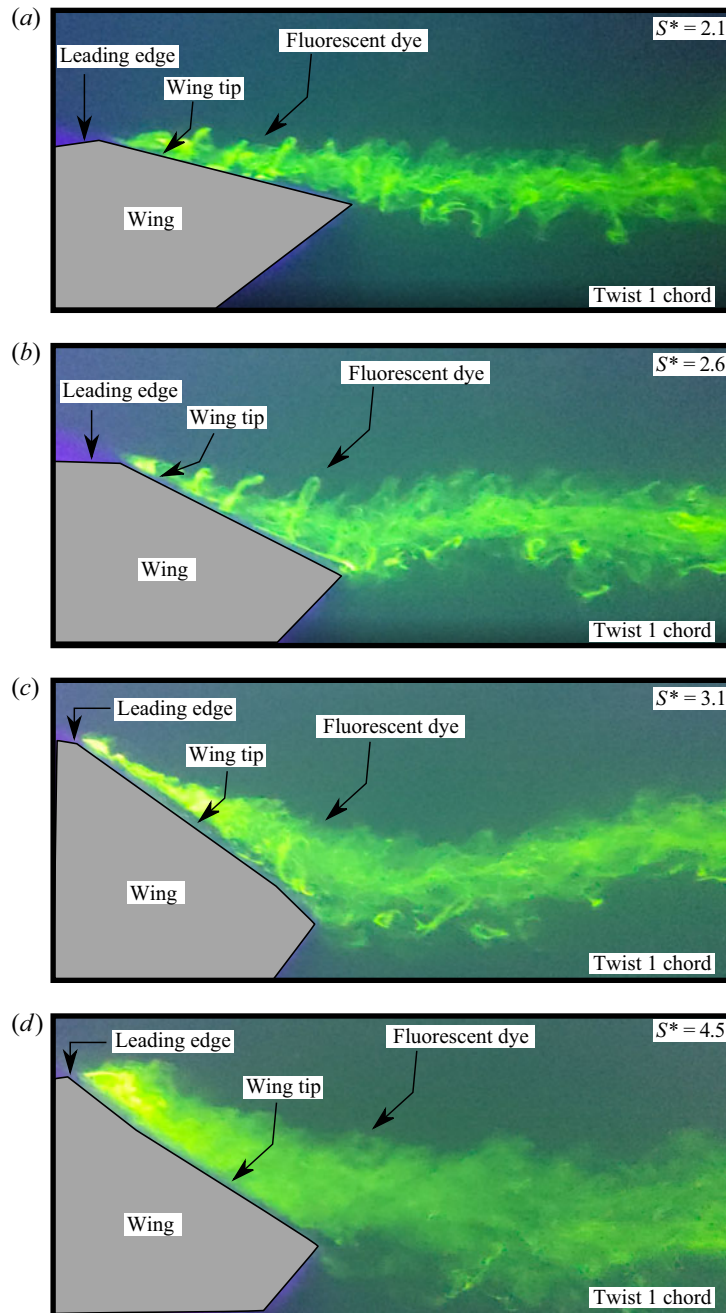


Figure 11. Dye visualisation of the tip vortex in the twist-1-chord case for an initial $AoA = 15^\circ$ at different S^* values.

straight case) begins as soon as the twisting manoeuvre starts. In contrast, for the LEV circulations, the change is not instantaneous and occurs after a chord length of travel at 86 % span and after two chord lengths of travel at 68 % span. The instantaneous change in circulation of the tip vortex due to twisting is because of the sudden kink in the axis of the vortex due to twisting. This kink bends the vortex and brings a larger portion of it

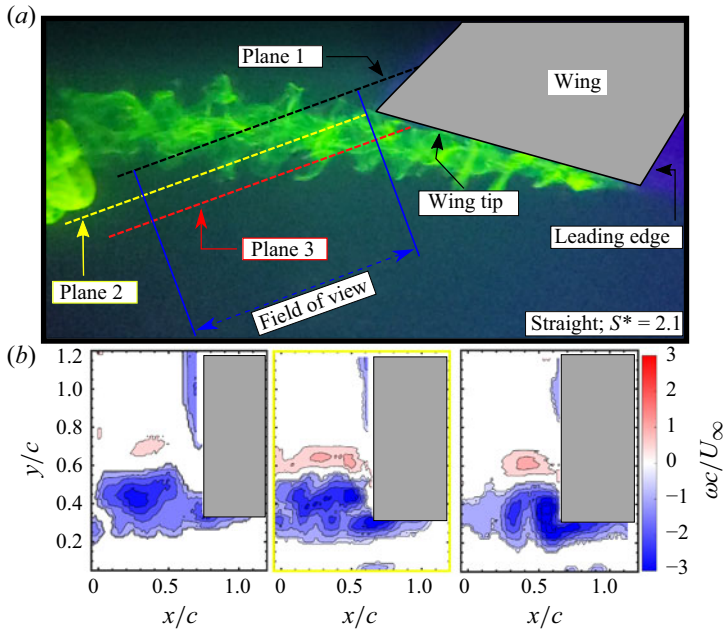


Figure 12. (a) The three cross-sectional planes cutting the tip vortex in the non-twisting case for initial AoA = 15° and at $S^* = 2.1$. (b) The contours of vorticity.

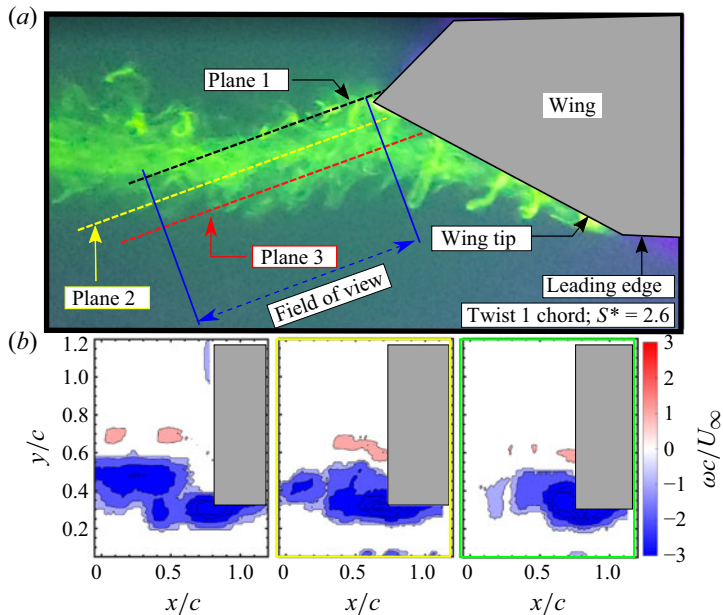


Figure 13. (a) The three cross-sectional planes cutting the tip vortex in the twist-1-chord case for initial AoA = 15° and at $S^* = 2.6$. (b) The contours of vorticity.

inside the measurement plane. This aspect is clear from figures 12 and 13 where a larger concentration of dye is present inside the measurement region in the latter figure.

The response to the twisting motion varies along the span. The increase in the growth of circulation near the tip (at 75 % and 86 % span locations) is higher than those away from the tip (at 68 % and 60 % span locations). Also, in most cases, the circulation starts peaking

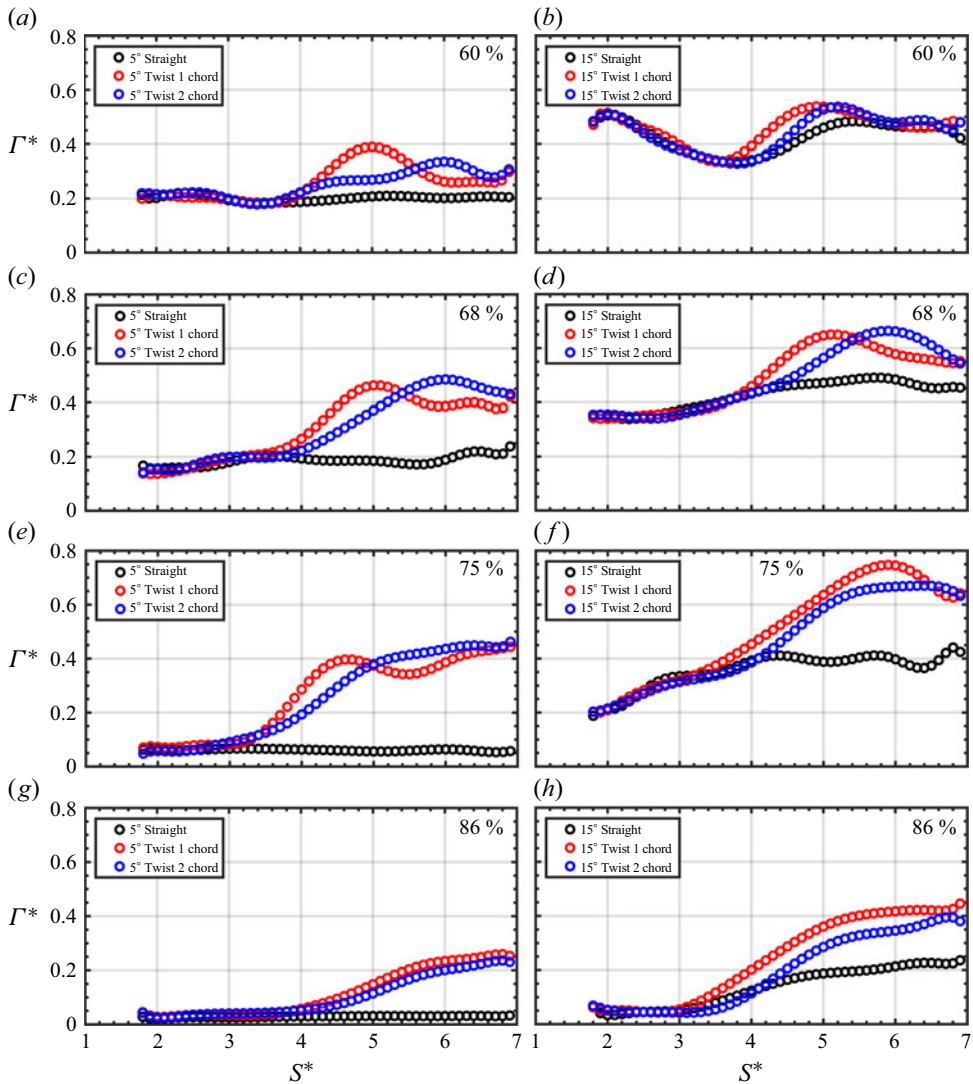


Figure 14. The comparison of circulation growths at 60 %, 68 %, 75 % and 86 % span. The left column represents $\text{AoA} = 5^\circ$ (a,c,e,g) and the right column represents $\text{AoA} = 15^\circ$ (b,d,f,h).

after one and two chord lengths of travel. Circulation reaches a maximum for the twist-1-chord case (red trace) at 75 % span when the AoA is 15° . This variation in response time underscores the complex 3-D nature of the flow field during spanwise twisting manoeuvres. There is probably a significant amount of spanwise vorticity transport that planar PIV could not capture.

3.5. Force partitioning

A dynamically twisting plate involves a moving surface which causes an increased level of vortical activity closer to the tip region. As such, we expect some kinematic contribution in addition to higher levels of circulatory forces in such twisting cases. In this section, we use the method of force partitioning, following Menon & Mittal (2021), to quantify the

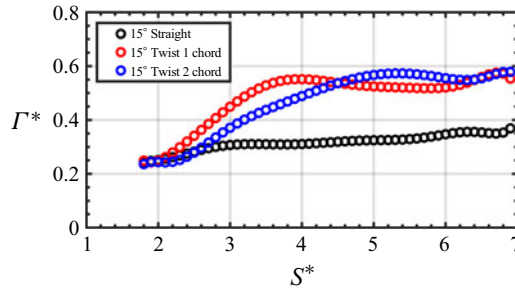


Figure 15. The growth of circulations in the tip vortex.

contribution of different factors to the total forces. First, we provide a quick overview of the force partitioning method. More details can be found in Menon & Mittal (2021) or in Zhang, Hedrick & Mittal (2015). The process begins with the construction of a 2-D auxiliary potential field, and then consideration of the gradient ($\nabla\phi_i$) aligned with the direction of interest – in this case, the direction of lift. The auxiliary potential field is a biharmonic function which is constructed to filter out the vectors along a generalised direction. In the context of hydrodynamics, this direction is often chosen to align with the lift, drag or moment vector. This auxiliary potential is obtained by solving the Laplace equation

$$\nabla^2(\Phi) = 0. \quad (3.1)$$

The boundary conditions are

$$\text{on the body surface} \rightarrow n \cdot \nabla(\Phi)_i = n_i, \quad (3.2a)$$

$$\text{at far field} \rightarrow n \cdot \nabla(\Phi)_i = 0. \quad (3.2b)$$

Here, n_i is the unit vector along a desired direction i . Next, we project the Navier–Stokes (NS) equation along $\nabla(\Phi)_i$. This projection is carried out by calculating the following volume integral:

$$\int_{V_f} ([\text{NS equation}] \cdot \nabla\Phi_i) dV. \quad (3.3)$$

In a broader sense, the result of this integral will show what is the relative contribution of each term of the NS equation, i.e. local acceleration, convective acceleration, pressure gradient and viscous stresses, towards the generation of a certain force field over a body.

The auxiliary potentials are computed using a MATLAB code developed by He & Zhu (2024). The forces acting on the body are then partitioned by projecting the relevant components onto the NS equation, followed by a volume integral over the fluid domain. The resulting force partitioning is expressed in terms of non-dimensional force coefficients, C_i , where $C_i = F_i / ((1/2)\rho U_\infty^2 c)$ represents the force coefficient in the i th direction, with F_i as the dimensional form of the force. This force can then be further divided into components corresponding to different force-producing mechanisms, as outlined below

$$C_i = C_\kappa^{(i)} + C_\omega^{(i)} + C_\sigma^{(i)} + C_\phi^{(i)} + C_\Sigma^{(i)}. \quad (3.4)$$

In this context, $C_\kappa^{(i)}$ denotes the kinematic force, while $C_\omega^{(i)}$ signifies the force induced by vorticity. The term $C_\sigma^{(i)}$ refers to the force resulting from viscous effects, and $C_\phi^{(i)}$ represents the force linked to the corresponding potential flow field. Additionally, $C_\Sigma^{(i)}$

accounts for the influence of the outer boundary. For our experiment, we assume that both $C_\sigma^{(i)}$ and $C_\Sigma^{(i)}$ are equal to zero

$$C_\kappa^{(i)} = - \int_B \mathbf{n} \cdot \frac{d\mathbf{U}_B}{dt} \phi_i dS - \int_B \frac{1}{2} |\mathbf{U}_B|^2 n_i dS, \quad (3.5)$$

$$C_\omega^{(i)} = \int_{V_f} [\nabla \cdot (\boldsymbol{\omega} \times \mathbf{u})] \phi_i dV + \int_{V_f} \nabla \cdot \left(\frac{1}{2} \mathbf{u}_v \cdot \mathbf{u}_v + \mathbf{u}_\phi \cdot \mathbf{u}_v \right) \phi_i dV, \quad (3.6)$$

$$C_\phi^{(i)} = \int_{V_f} \nabla \cdot \left(\frac{1}{2} \mathbf{u}_\phi \cdot \mathbf{u}_\phi \right) \phi_i dV, \quad (3.7)$$

where U_B represents the velocity of the wing at the local PIV plane, while ϕ_i is the auxiliary potential field in the i th direction, determined by the wing's position. The vorticity $\boldsymbol{\omega}$ and velocity \mathbf{u} fields are derived from PIV data at a specific span. Here, U_v and U_ϕ are the rotational and irrotational components of the velocity field, respectively, obtained from the PIV experiments using Helmholtz decomposition (Wu, Ma & Zhou 2015). The integral over the control volume is computed assuming a unit depth in the spanwise direction.

To perform the Helmholtz decomposition to separate rotational and irrotational velocity components, we have first discretised the Helmholtz equations

$$\mathbf{U} = -\nabla\phi + \nabla \times \psi. \quad (3.8)$$

Divergent component

$$U_{div} = \frac{\phi(i, j) - \phi(i-1, j)}{\Delta x}, \quad (3.9)$$

$$V_{div} = \frac{\phi(i, j) - \phi(i, j-1)}{\Delta y}. \quad (3.10)$$

Rotational component

$$U_{rot} = \frac{\psi(i, j+1) - \psi(i, j)}{\Delta y}, \quad (3.11)$$

$$V_{rot} = \frac{\psi(i+1, j) - \psi(i, j)}{\Delta x}. \quad (3.12)$$

Then, a linear system is formed, which is solved implicitly

$$A \begin{bmatrix} \phi \\ \psi \end{bmatrix} = \begin{bmatrix} U \\ V \end{bmatrix}. \quad (3.13)$$

We used MATLAB's `mldivide` (backslash operator) to solve the linear system. This operator uses Lower Upper factorisation to compute the solution.

Figure 16 presents a comparison of results for two spanwise planes: 68 % (figures 16a, 16c and 16e) and 86 % span (figures 16b, 16d and 16f) for the $\text{AoA} = 15^\circ$. The results indicate that the forces induced by vorticity are greater at the 86 % span compared with the 68 % span for both twisting manoeuvres. This increase in C_ω is attributed to enhanced vortex growth closer to the tip region of the plate due to the twisting manoeuvre. Furthermore, it also proves that dynamic twisting allows us to alter the spanwise distribution of circulation. The kinematic contribution to the forces increases during the period of twisting as the plate boundary moves through the domain. This is evident in figures 16(d) and 16(f).

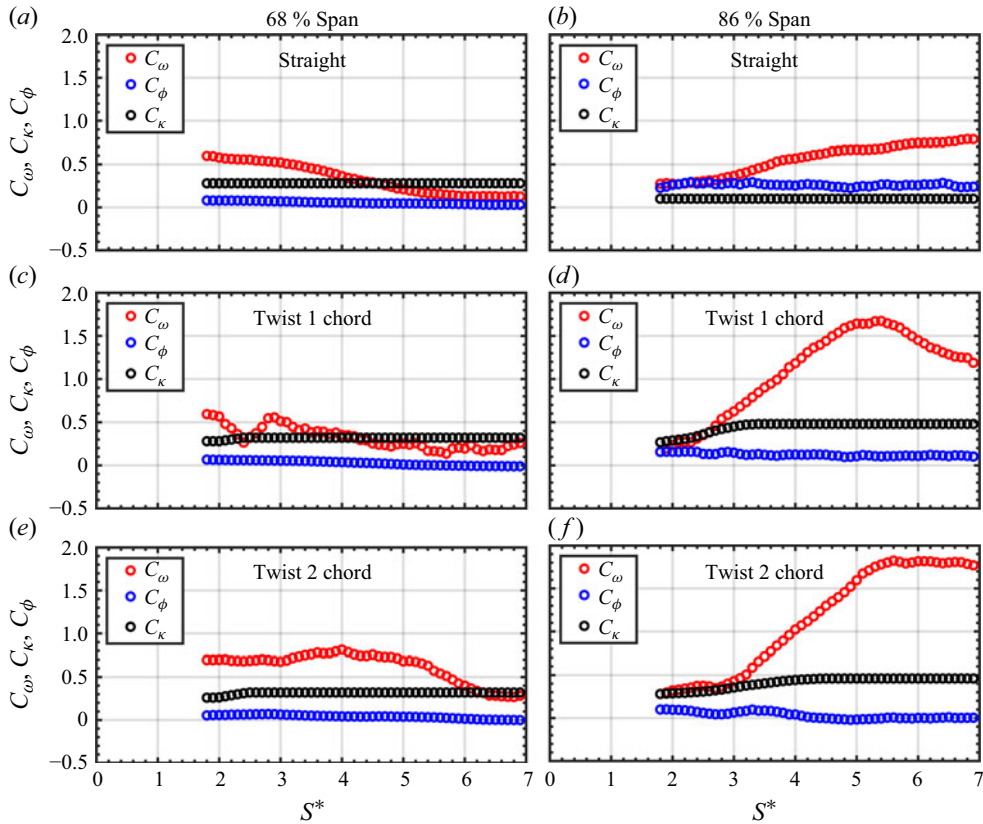


Figure 16. The force contributions from kinematics (C_κ), vorticity-induced effects (C_ω) and irrotational effects (C_ϕ) for two spanwise planes: 68 % (a,c,e) and 86 % (b,d,f), for the no-twist case, twist-1-chord case and twist-2-chord case.

We note that this force partitioning approach does not take into account the three-dimensionality of the flow. However, force partitioning can be applied to 3-D volumetric data as well, which we lack. The use of 2-D force partitioning surely can not capture 3-D effects but it can capture the differences in the vorticity-induced force along the span of a dynamically twisting wing. But for a twisting plate, the tip vortex changes location dynamically with respect to the midspan. Hence, a change in the tip-vortex-induced force is expected for such kinematics. Such a dynamic change in the downwash may lead to spanwise flows, which the present work could not capture.

4. Analytical model

The analytical model presented here has two major parts. The first part employs the LDVM developed by Ramesh *et al.* (2014). In the second part, we use the methodology prescribed by Faure & Leogrande (2020) which extended the LDVM developed by Ramesh *et al.* (2014) to a finite wing. Our unique contribution to this modelling is that we modify the second part and implement a strip theory approach where the AoA of each strip is varied with time. By using such a spanwise non-uniform, time-varying AoA, we model the effect of dynamic twisting on the resultant unsteady forces.

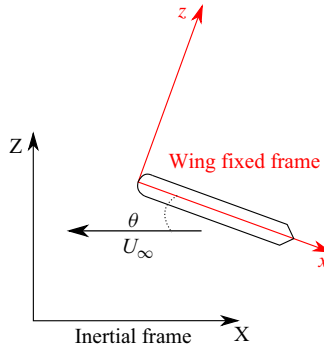


Figure 17. Wing reference frame and the inertial frame.

4.1. Brief summary of LDVM

The LDVM is based on the time-stepping approach described in Katz & Plotkin (2001). In this method, a wing with chord ‘ c ’ is situated in a free-stream flow with velocity U_∞ as illustrated in figure 17. The wing’s frame of reference is represented by x – z , while the inertial frame of reference is denoted by X – Z . The variable ϑ is used to transform the chordwise coordinates along the x -axis

$$x = \frac{c}{2}(1 - \cos \vartheta). \quad (4.1)$$

The vorticity distribution $\gamma(\vartheta, t)$ along the x -axis is expressed in terms of the Fourier series

$$\gamma(\vartheta, t) = 2U_\infty \left[A_o(t) \frac{1 + \cos \vartheta}{\sin \vartheta} + \sum_{n=1}^{\infty} A_n \sin n\vartheta \right]. \quad (4.2)$$

Here, A_o and A_n represent the Fourier coefficients, which are computed using the velocity component W normal to the wing, which is set to zero to enforce the no-penetration boundary conditions along the wing

$$A_o(t) = \frac{-1}{\pi} \int_0^\pi \frac{W(\vartheta, t)}{U_\infty} d\vartheta, \quad n = 0, \quad (4.3a)$$

$$A_n(t) = \frac{2}{\pi} \int_0^\pi \frac{W(\vartheta, t)}{U_\infty} \cos n\vartheta d\vartheta, \quad n = 1, 2, 3 \dots \quad (4.3b)$$

The normal velocity induced to the airfoil is calculated from (4.4)

$$\begin{aligned} W(x, t) = & \left[\frac{\partial \phi_L}{\partial x}(x, t) + \frac{\partial \phi_T}{\partial x}(x, t) + U_\infty \cos \theta(t) + \dot{h} \sin \theta(t) \right] \frac{\partial \eta}{\partial x}(x, t) \\ & - \frac{\partial \phi_L}{\partial z}(x, t) - \frac{\partial \phi_T}{\partial z}(x, t) - U_\infty \sin \theta(t) \\ & - \dot{\theta}(t)(x - x_p) + \dot{h} \cos \theta(t). \end{aligned} \quad (4.4)$$

Here, η represents the wing camber line, while ϕ_L and ϕ_T denote the velocity potentials for the LEV and TEV, respectively. The pivot location is defined as x_p , and $\dot{\theta}$ refers to the time derivative of the AoA, with \dot{h} corresponding to the plunging velocity in the Z direction. The TEVs are shed at each time step, and their strengths are determined

iteratively following Kelvin's circulation theorem

$$\Gamma_B + \sum_{k=1}^i \Gamma_{T,k} + \sum_{l=1}^i \Gamma_{L,l} = 0, \quad (4.5)$$

where Γ_B represents the bound circulation obtained by integrating the chordwise distribution of bound vorticity over the airfoil chord

$$\Gamma_B = U_\infty c \pi \left[A_o(t) + \frac{A_1(t)}{2} \right]. \quad (4.6)$$

To initiate the formation of LEV, we employ the LESP criterion, which is a non-dimensional measure of suction at the leading edge and is given by

$$LESP(t) = A_o(t). \quad (4.7)$$

If the LESP at a certain time, denoted as LESP(t), exceeds the critical LESP value, LEV shedding occurs. In such cases, both LEV and TEV strengths are recalculated. The implementation of these two criteria ((4.5) and (4.7)) within the discrete vortex method has been previously demonstrated by Ramesh *et al.* (2014). For calculating the velocities induced by the LEV, TEV and bound vortex, we utilise the vortex core model proposed by Vastistas, Kozel & Mih (1991)

$$u = \frac{\gamma_o}{2\pi} \frac{X - X_o}{\sqrt{((X - X_o)^2 + (Z - Z_o)^2)^2 + r_c^4}}, \quad (4.8a)$$

$$w = \frac{\gamma_o}{2\pi} \frac{Z - Z_o}{\sqrt{((X - X_o)^2 + (Z - Z_o)^2)^2 + r_c^4}}, \quad (4.8b)$$

where u and w are the velocities induced by the vortex in the inertial frame of reference X and Z . For more comprehensive details regarding the LDVM and load calculation, we direct readers to Ramesh *et al.* (2014).

4.2. Brief summary of three-dimensional LDVM for finite wing

According to Lifting Line Theory (Houghton & Carpenter 2003), the wing is modelled as a distribution of horseshoe vortices along its span

$$\Gamma(\phi, t) = 2bU_\infty(t) \sum_{n=1}^N P_n(t) \sin n\phi, \quad (4.9)$$

where ϕ is the parameter defined along the span b

$$y = \frac{-b}{2} \cos \phi. \quad (4.10)$$

The downwash at a specific spanwise station y , which corresponds to a parameter ϕ resulting from all the shed filaments, is given by

$$W_i(\phi, t) = -U_\infty \sum_{n=1}^N n P_n(t) \frac{\sin n\phi}{\sin \phi}. \quad (4.11)$$

The coupling of 2-D LDVM and lifting line theory has been accomplished due to their shared foundation in potential flow principles, as highlighted by Faure &

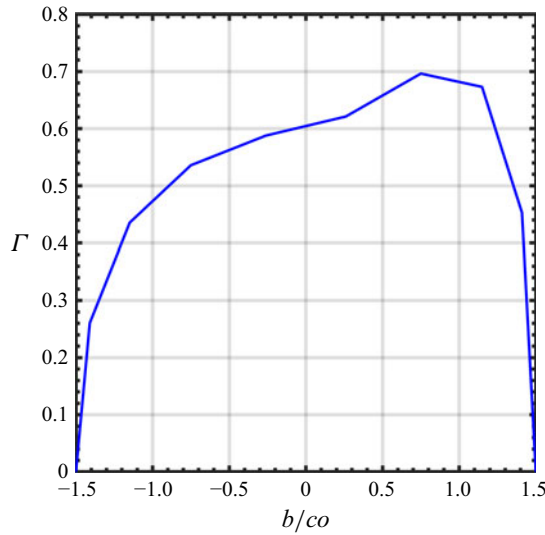


Figure 18. Circulation distribution for the twisted wing along the span using lifting line theory.

Leogrande (2020). The underlying potential flow nature is characterised by the solution of the Laplace equation. To integrate these models effectively, we apply the superposition principle, combining potential functions from different potential flows. As a result, the velocities are added together, leading to the expression $W = (\partial\Phi)/(\partial z)$

$$W(t) = W_{2D}(\vartheta, t) + W_i(\phi, t). \quad (4.12)$$

The time-dependent Fourier series coefficient from LESP and thin airfoil theory are combined, which results in chordwise circulation at each strip as

$$\Gamma(\phi, t) = U_\infty c \pi \left[A_{0,2D}(t) + A_{0,3D}(t) + \frac{A_{1,2D}(t)}{2} \right], \quad (4.13)$$

where $A_{03D}(t) = \sum_{n=1}^N n P_n(t)(\sin n\phi/\sin \phi)$.

4.3. Adding AoA variation to model spanwise twisting

To implement spanwise twisting, we initially incorporate the spanwise AoA variation in the lifting line theory. The case of $\text{AoA} = \theta$ is defined along the wing's span as

$$\theta(\phi, t) = \theta_m + \theta_{twist}(\phi, t), \quad (4.14)$$

where θ_m represents the AoA for the straight wing, which is set to be 5° and 15° in our study. Here, θ_{twist} denotes the spanwise twist introduced along the wing's span. Notably, the twist variations remain consistent for both 5° and 15° AoA cases. We determine these twist variations using the DLTdv digitising tool (refer to § 2.3 for more detail). The Fourier coefficient for the lifting line theory at an instant t_1 can be calculated using (4.15), yielding

$$\theta(\phi, t = t_1) = \sum_{n=1}^{\infty} n A_n \frac{\sin n\phi}{\sin \phi}. \quad (4.15)$$

As a result of introducing θ_{twist} , the circulation distribution becomes asymmetric once the twisting manoeuvre starts. Figure 18 illustrates the circulation distribution after the twisting manoeuvre starts at a 15° AoA, which is plotted using (4.9).

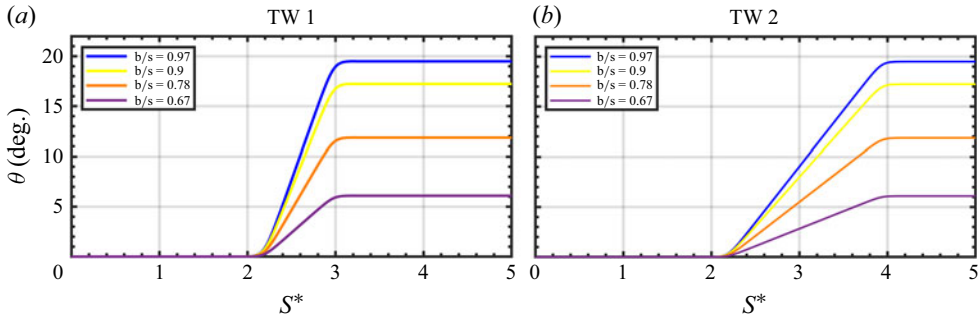


Figure 19. The θ_{twist} values used for the analytical model. These values are simplified using the Eldredge function. Panels show (a) TW1 and (b) TW2.

To incorporate the twisting manoeuvre (θ_{twist} and $\dot{\theta}_{twist}$) into the analytical model, we used the Eldredge function (Eldredge 2007) with a smoothing parameter of $a = 11$, which applies to both twist-1 and twist-2 chords. Additionally, for the twist-1-chord, we employed a non-dimensional pitch rate ($K = \dot{\theta}_{twist}c/2U_\infty$) of $K = 0.2$, while for the twist-2-chord, we utilised a non-dimensional pitch rate of $K = 0.1$. Figures 2 and 19 show the comparison of θ_{twist} between the experimental and theoretical models for twist-1 and twist-2 chords, respectively. When comparing the results with experimental data, we note that θ_{twist} in the analytical model is smoother than its experimental counterpart.

For each spanwise strip, we independently conduct the LDVM analysis based on the corresponding twisting angle associated with that strip. As a result, there is a variation in the circulation term in (4.13) due to these individual twistings

$$\Gamma(\phi, t) = U_\infty c \pi \left[A_{0,2D}(\phi, t) + A_{0,3D}(\phi, t) + \frac{A_{1,2D}(\phi, t)}{2} \right]. \quad (4.16)$$

4.4. Determination of critical LESP

We first performed an iteration of our LDVM code with a range of critical LESP values with the goal of matching the force sensor data for the twist-1-chord for the 15° AoA case. We obtained the best match for critical LESP of 0.21. We then kept this value constant for all other kinematics. This approach has also been described on p. 532 of Ramesh *et al.* (2014).

4.5. Lift force comparison with analytical model

In this section, we compare the experimental data to the analytical model discussed in §4.3. Figures 20 and 21 illustrate the comparison for AoAs 5° and 15° of the AR3 wing, respectively. The results demonstrate that the analytical model closely predicted the trend in the variation of lift coefficient during the twisting manoeuvres for both twist-1 and twist-2 chords. However, it is worth noting that the experimental data exhibited higher fluctuations in both cases. These fluctuations were attributed to the sudden onset of the twist manoeuvre and the overall higher variability observed throughout the twisting manoeuvre (refer to figure 2). Such behaviour is not modelled due to the simplification of the twisting manoeuvre achieved by utilising the Eldredge function.

The LDVM yields a potential flow field with discrete point vortices representing the LEV and TEVs. The trajectories of these point vortices create a flow field over the plate and in the wake. Such flow fields of point vortices are compared with the vorticity contours obtained experimentally in figure 22. Here, we only show the straight (figures 22a and 22b)

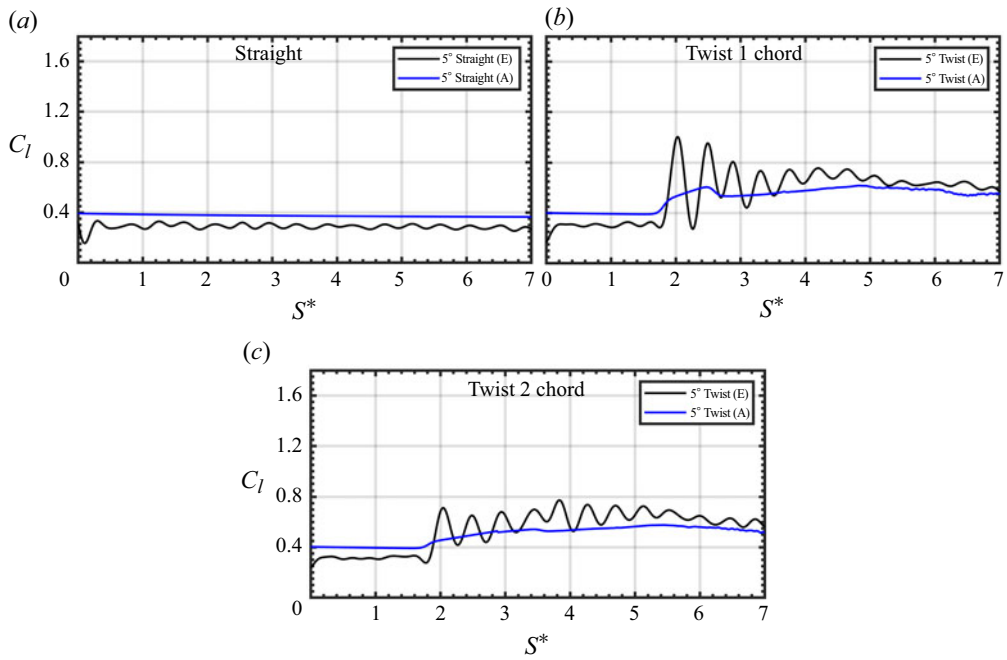


Figure 20. The comparison of experimental and analytical results for the twisting manoeuvre for the AR3 wing at an AoA 5° .

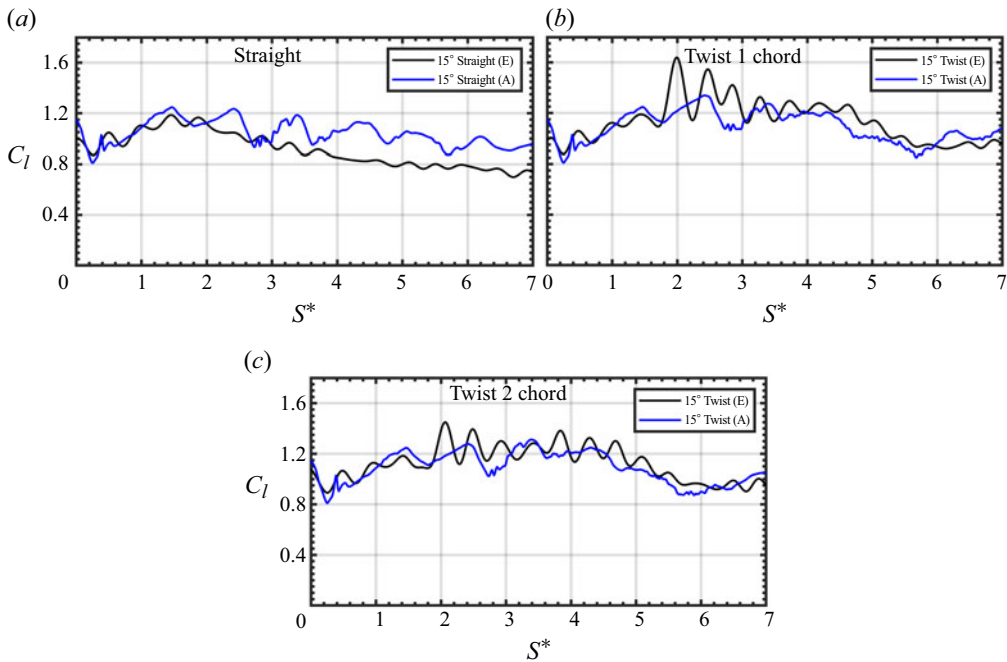


Figure 21. The comparison of experimental and analytical results for the twisting manoeuvre for the AR3 wing at an AoA 15° .

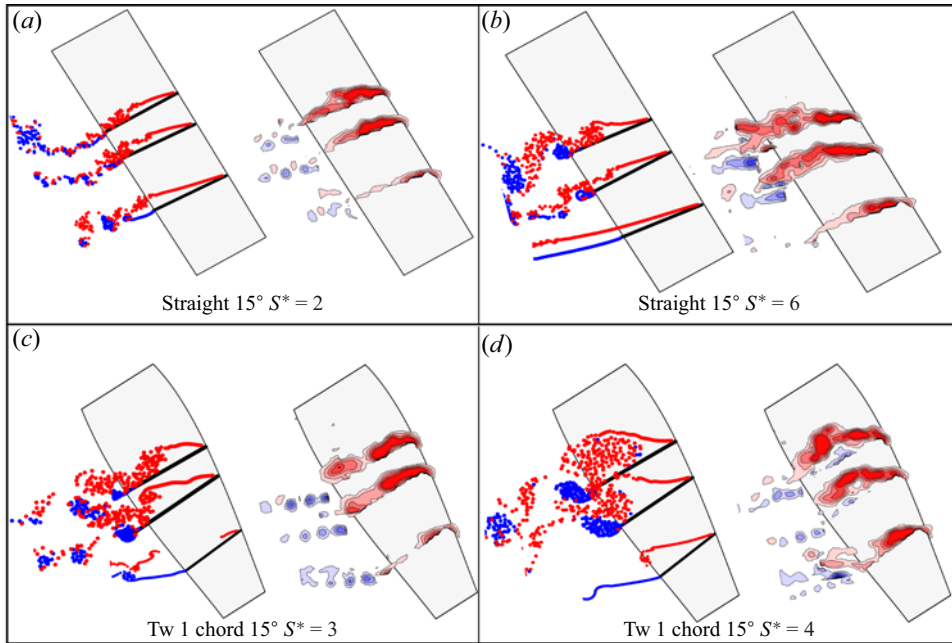


Figure 22. Flow feature comparison between LDVM and PIV results at 75 %, 81 % and 90 % span. Panels (a) and (b) show the straight wing at $s^* = 2$ and 6, respectively. Panels (c) and (d) show the twisted wing (1 chord) at $s^* = 3$ and 4, respectively.

and the twist-1-chord cases (figures 22c and 22d). The LDVM computation correctly models the gradual decay of circulation towards the span in both cases. The massive separation and eventual roll-up of the LEV is also captured by the LDVM in the twisting case at 75 % span (figure 22d).

5. Conclusion

We measured the instantaneous forces and the flow field of a flat-plate wing, which was dynamically twisted along the span while translating at a Re value of 10 000. In addition to experimental measurements, we also implemented a discrete vortex model that incorporated the LESP to account for the unsteady forces on a dynamically twisting plate. Experiments were conducted for two AoAs, namely, 5° and 15° , and two twist rates. In the first case, the wing was twisted to the maximum tip AoA during one chord length of travel. In the second case, a slower twist rate was applied where the wing was twisted to the maximum tip AoA during two chord lengths of travel. In both these cases, the wing leading edge was twisted away from the incoming flow, or the direction of twist was opposite to the direction of motion. Our results show that spanwise twisting increases the lift forces significantly. The lift-to-drag ratio improves the most for the higher twist rate case (the twist-1-chord case). The most pronounced effects were observed at higher AoAs of 15° . The increase in the effective AoA promoted the formation of LEV over the twisted part closer to the tip. Such vortex formation close to the tip was hardly observed in the case without twisting. The circulation inside the LEV was increased due to twisting. The rate of increase of circulation was higher in the higher twist rate case. Although a dip in the growth of circulation was observed, which was related to the early shedding of the LEV.

Through our force partitioning analysis, we showed that the increasing vortical presence during dynamic twisting led to a localised increase in vorticity-induced forces, particularly near the twisted section of the plate. It underscores the significant role of active morphing in controlling unsteady flow behaviour. Our discrete vortex model with LESP effectively captured this dynamics, demonstrating its potential as a low-order tool for predicting the complex interactions between twisting kinematics and vortex formation.

Our study advances the understanding of the mechanisms underlying the hydrodynamic benefits of active morphing in natural and artificial flyers. We believe that controlled spanwise twisting can be leveraged to enhance aerodynamic performance, reduce drag and manipulate vortex-shedding patterns, paving the way for improved designs of bio-inspired propulsion systems and control surfaces. In future research, we aim to refine our model to account for 3-D flow effects and explore the implications of twist-induced flow structures on energy efficiency and manoeuvrability in more complex configurations.

Acknowledgements. This work was supported by the National Science Foundation CAREER award 2045767 and monitored by Dr. R.D. Joslin. We thank Dr. Y. Zhu for pointing us to his MATLAB codes for the calculation of auxiliary potential.

Declaration of interests. The authors report no conflict of interest.

REFERENCES

- BOUARD, F., JARDIN, T. & DAVID, L. 2024 Aerodynamics of flapping wings with passive and active deformation. *J. Fluids Struct.* **128**, 104139.
- CAVANAGH, A., BOSE, C. & RAMESH, K. 2024 Effect of sweep angle on three-dimensional vortex dynamics over plunging wings. [arXiv:2407.04972](https://arxiv.org/abs/2407.04972)
- COMBES, S.A. & DANIEL, T.L. 2003 Flexural stiffness in insect wings II. Spatial distribution and dynamic wing bending. *J. Expl Biol.* **206** (17), 2989–2997.
- CONG, L., TENG, B., CHEN, L., BAI, W., JIN, R. & CHEN, B. 2023 Aerodynamic performance of low aspect-ratio flapping wing with active wing-chord adjustment. *J. Fluids Struct.* **122**, 103964.
- DANIEL, T.L. & COMBES, S.A. 2002 Flexible wings and fins: bending by inertial or fluid-dynamic forces? *Integr. Compar. Biol.* **42** (5), 1044–1049.
- DICKINSON, M.H., LEHMANN, F.-O. & CHAN, W. P. 1998 The control of mechanical power in insect flight. *Am. Zool.* **38** (4), 718–728.
- DICKINSON, M.H., LEHMANN, F.-O. & SANE, S.P. 1999 Wing rotation and the aerodynamic basis of insect flight. *Science* **284** (5422), 1954–1960.
- DONG, Y., SONG, B., YANG, W. & XUE, D. 2024 A numerical study on the aerodynamic effects of dynamic twisting on forward flight flapping wings. *Bioinspir. Biomim.* **19** (2), 026013.
- DUDLEY, R. 2002 *The Biomechanics of Insect Flight: Form, Function, Evolution*. Princeton University Press.
- ELDRIDGE, J.D. 2007 Numerical simulation of the fluid dynamics of 2D rigid body motion with the vortex particle method. *J. Comput. Phys.* **221** (2), 626–648.
- ELLINGTON, C.P. 1999 The novel aerodynamics of insect flight: applications to micro-air vehicles. *J. Expl Biol.* **202** (23), 3439–3448.
- FAURE, T.M. & LEOGRANDE, C. 2020 High angle-of-attack aerodynamics of a straight wing with finite span using a discrete vortex method. *Phys. Fluids* **32** (10), 104109-1–104109-10.
- GRAFTIEAUX, L., MICHARD, M. & GROSJEAN, N. 2001 Combining PIV, POD and vortex identification algorithms for the study of unsteady turbulent swirling flows. *Meas. Sci. Technol.* **12** (9), 1422.
- GRODNITSKY, D.L. & MOROZOV, P.P. 1993 Vortex formation during tethered flight of functionally and morphologically two-winged insects, including evolutionary considerations on insect flight. *J. Expl Biol.* **182** (1), 11–40.
- HE, X. & ZHU, Y. 2024 Force and moment partitioning influence potential solver 2D-MATLAB-Central File Exchange. Available at: <https://www.mathworks.com/matlabcentral/fileexchange/130274-force-and-moment-partitioning-influence-potential-solver-2d>. Retrieved September 27, 2024.
- HEATHCOTE, S. & GURSUL, I. 2007 Flexible flapping airfoil propulsion at low Reynolds numbers. *AIAA J.* **45** (5), 1066–1079.
- HEATHCOTE, S., WANG, Z. & GURSUL, I. 2008 Effect of spanwise flexibility on flapping wing propulsion. *J. Fluids Struct.* **24** (2), 183–199.
- HOUGHTON, E.L. & CARPENTER, P.W. 2003 *Aerodynamics for Engineering Students*. Elsevier.

- INGERSOLL, R. & LENTINK, D. 2018 How the hummingbird wingbeat is tuned for efficient hovering. *J. Expl Biol.* **221** (20), jeb178228.
- JONGERUS, S.R. & LENTINK, D. 2010 Structural analysis of a dragonfly wing. *Expl Mech.* **50**, 1323–1334.
- KANG, C.-K., AONO, H., CESNIK, C.E.S. & SHYY, W. 2011 Effects of flexibility on the aerodynamic performance of flapping wings. *J. Fluid Mech.* **689**, 32–74.
- KATZ, J. & PLOTKIN, A. 2001 *Low-Speed Aerodynamics*, 2nd edn. Cambridge Aerospace Series 1. Cambridge University Press.
- KUMAR, R., PADHEE, S.S. & SAMANTA, D. 2024 Aerodynamic performance and flow mechanism of 3D flapping wing using discrete vortex method. *J. Fluids Struct.* **127**, 104128.
- LEISHMAN, J.G. 1989 State-space model for unsteady airfoil behavior and dynamic stall. In *30th Structures, Structural Dynamics and Materials Conference*, pp. 1319. American Institute of Aeronautics and Astronautics, Inc.
- LEISHMAN, J.G. & BEDDOES, T.S. 1989 A semi-empirical model for dynamic stall. *J. Am. Helicopter Soc.* **34** (3), 3–17.
- LENTINK, D., *et al.* 2007 How swifts control their glide performance with morphing wings. *Nature* **446** (7139), 1082–1085.
- LINEHAN, T. & MOHSENI, K. 2020 On the maintenance of an attached leading-edge vortex via model bird alula. *J. Fluid Mech.* **897**, A17.
- MARTÍNEZ-CARMENA, A. & RAMESH, K. 2024 Inviscid modeling of unsteady morphing airfoils using a discrete-vortex method. *Theor. Comput. Fluid Dyn.* **38** (6), 845–862.
- MENON, K. & MITTAL, R. 2021 On the initiation and sustenance of flow-induced vibration of cylinders: insights from force partitioning. *J. Fluid Mech.* **907**, A37.
- NAKATA, T. & LIU, H. 2012 Aerodynamic performance of a hovering hawkmoth with flexible wings: a computational approach. *Proc. R. Soc. B: Biol. Sci.* **279** (1729), 722–731.
- NODA, R., NAKATA, T. & LIU, H. 2014 Effects of wing deformation on aerodynamic performance of a revolving insect wing. *Acta Mechanica Sin.* **30**, 819–827.
- PLA OLEA, L. & TAHA, H.E. 2024 Geometric control analysis of the unsteady aerodynamics of a pitching–plunging airfoil in dynamic stall. *Phys. Fluids* **36** (3), 037116–1–037116–13.
- RAMESH, K., GOPALARATHNAM, A., GRANLUND, K., OL, M.V. & EDWARDS, J.R. 2014 Discrete-vortex method with novel shedding criterion for unsteady aerofoil flows with intermittent leading-edge vortex shedding. *J. Fluid Mech.* **751**, 500–538.
- SON, O., GAO, A.-K., GURSUL, I., CANTWELL, C.D., WANG, Z. & SHERWIN, S.J. 2022 Leading-edge vortex dynamics on plunging airfoils and wings. *J. Fluid Mech.* **940**, A28.
- SOTO, C. & BHATTACHARYA, S. 2023 The effect of dynamic twisting on the flow field and the unsteady forces of a heaving flat plate. *Bioinspir. Biomim.* **18** (2), 026010.
- STAMHUIS, E. & THIELICKE, W. 2014 PIVlab – towards user-friendly, affordable and accurate digital particle image velocimetry in MATLAB. *J. Open Res. Softw.* **2** (1), 30.
- TAHA, H.E., HAJJ, M.R. & BERAN, P.S. 2014 State-space representation of the unsteady aerodynamics of flapping flight. *Aerosp. Sci. Technol.* **34**, 1–11.
- TAHA, H.E., PLA OLEA, L., KHALIFA, N., GONZALEZ, C. & REZAEI, A.S. 2021 Geometric-control formulation and averaging analysis of the unsteady aerodynamics of a wing with oscillatory controls. *J. Fluid Mech.* **928**, A30.
- TU, Y., WANG, J., HU, H. & DONG, H. 2020 Twist morphing effect on propulsive performance of bio-inspired pitching-rolling plates. In *AIAA Scitech 2020 Forum*, pp. 2019.
- VATISTAS, G.H., KOZEL, V. & MIH, W.C. 1991 A simpler model for concentrated vortices. *Exp. Fluids* **11** (1), 73–76.
- WEI, W., WEIGANG, A. & BIFENG, S. 2024 Effect of wing morphing on stability and energy harvesting in albatross dynamic soaring. *Chin. J. Aeronaut.* **37** (11), 317–334.
- WOOTTON, R. 2020 The geometry and mechanics of insect wing deformations in flight: a modelling approach. *Insects* **11** (7), 446.
- WU, J.-Z., MA, H.-Y. & ZHOU, M.-D. 2015 *Vortical Flows*, vol. 28. Springer.
- YAN, Z., TAHA, H.E. & HAJJ, M.R. 2014 Geometrically-exact unsteady model for airfoils undergoing large amplitude maneuvers. *Aerosp. Sci. Technol.* **39**, 293–306.
- ZHANG, C., HEDRICK, T.L. & MITTAL, R. 2015 Centripetal acceleration reaction: an effective and robust mechanism for flapping flight in insects. *PLoS One* **10** (8), e0135571.
- ZHENG, L., HEDRICK, T.L., MITTAL, R. & AEGERTER, C.M. 2013 Time-varying wing-twist improves aerodynamic efficiency of forward flight in butterflies. *PloS One* **8** (1), e53060.